Article

Journal of Intelligent Material Systems and Structures

Journal of Intelligent Material Systems and Structures
23(13) 1505–1521
© The Author(s) 2012
Reprints and permissions:
sagepub.co.uk/journalsPermissions.nav
DOI: 10.1177/1045389X12455722
jim.sagepub.com
SAGE

Non-linear piezoelectric vibration energy harvesting from a vertical cantilever beam with tip mass

Michael I Friswell[1], S Faruque Ali[1], Onur Bilgen[1], Sondipon Adhikari[1], Arthur W Lees[1] and Grzegorz Litak[2]

Abstract

A common energy harvesting device uses a piezoelectric patch on a cantilever beam with a tip mass. The usual configuration exploits the linear resonance of the system; this works well for harmonic excitation and when the natural frequency is accurately tuned to the excitation frequency. A new configuration is proposed, consisting of a cantilever beam with a tip mass that is mounted vertically and excited in the transverse direction at its base. This device is highly non-linear with two potential wells for large tip masses, when the beam is buckled. The system dynamics may include multiple solutions and jumps between the potential wells, and these are exploited in the harvesting device. The electromechanical equations of motion for this system are developed, and its response for a range of parameters is investigated using phase portraits and bifurcation diagrams. The model is validated using an experimental device with three different tip masses, representing three interesting cases: a linear system; a low natural frequency, non-buckled beam; and a buckled beam. The most practical configuration seems to be the pre-buckled case, where the proposed system has a low natural frequency, a high level of harvested power and an increased bandwidth over a linear harvester.

Keywords

energy harvesting, piezoelectric, non-linear dynamics

Introduction

Energy harvesting of ambient vibration is important for remote devices, for example, in structural health monitoring (Anton and Sodano, 2007; Beeby et al., 2006; Lefeuvre et al., 2005, 2006; Priya, 2007; Sodano et al., 2004). Completely wireless sensor systems are desirable, and this can only be accomplished by using batteries and/or harvested energy. Harvesting is attractive because the energy generated can be used directly or used to recharge batteries or other storage devices, which enhances battery life. Most of the results using the piezoelectric effect as the transduction method have used cantilever beams and single frequency excitation, that is, resonance-based energy harvesting. The design of an energy harvesting device must be tailored to the ambient energy available. For single frequency ambient excitation, the resonant harvesting device is optimum, provided it is tuned to the excitation frequency. Ng and Liao (2005), duToit et al. (2005), Roundy (2005) and Renno et al. (2009) have proposed methods to optimise the parameters of the system to maximise the harvested energy. Shu and Lien (2006a, 2006b) and Shu et al. (2007) conducted a detailed analysis of the power output for piezoelectric energy harvesting systems.

Energy harvesting exploiting linear vibration has been investigated widely, and explicit expressions for optimal parameters are available in the literature (Erturk and Inman, 2011c). One of the drawbacks of linear energy harvesters is that generally they are efficient only when the excitation frequency is around the resonance frequency (Daqaq, 2010). Therefore, most linear energy harvesting devices are designed on the assumption that the (base) excitation has some known form, typically harmonic excitation. However, there are many situations where energy harvesting devices are operating under unknown or random excitations, and in such situations,

[1]College of Engineering, Swansea University, UK
[2]Department of Applied Mechanics, Lublin University of Technology, Lublin, Poland

Corresponding author:
Michael I Friswell, College of Engineering, Swansea University, Singleton Park, Swansea SA2 8PP, UK.
Email: m.i.friswell@swansea.ac.uk

harvesters with a broadband or adaptive response are likely to be beneficial. One approach is to adaptively change the parameters of the linear harvester, so that its natural frequency becomes close to the excitation frequency as it changes (Wang et al., 2009). Such adaptive systems may be difficult to implement in general and may not adapt well to a broadband excitation. Ferrari et al. (2008) used an array of cantilever beam harvesters tuned to different frequencies.

An alternative approach to maximise the harvested energy over a wide range of excitation frequency uses non-linear structural systems, and a range of devices have been proposed (Cottone et al., 2009; Gammaitoni et al., 2009, 2010). The key aspect of the non-linear harvesters is the use of a double potential well function, so that the device will have two equilibrium positions (Cottone et al., 2009; Ferrari et al., 2010; Mann and Owens, 2010; Quinn et al., 2011; Ramlan et al., 2010). Gammaitoni et al. (2009) and Masana and Daqaq (2011) highlighted the advantages of a double potential well for energy harvesting, particularly when inter well dynamics were excited. The simplest equation of motion with a double potential well is the well-known Duffing oscillator, which has been extensively studied, particularly for sinusoidal excitation. The dynamics is often complex, sometimes with coexisting periodic solutions and sometimes exhibiting a chaotic response. The Duffing oscillator model has been used for many energy harvesting simulations, with the addition of electromechanical coupling for the harvesting circuit. One popular implementation of such a potential is a piezomagnetoelastic system based on the magnetoelastic structure that was first investigated by Moon and Holmes (1979) as a mechanical structure that exhibits strange attractor motions. Erturk et al. (2009) investigated the potential of this device for energy harvesting when the excitation is harmonic and demonstrated an order of magnitude larger power output over the linear system (without magnets) for non-resonant excitation. One problem with multiple solutions to harmonic excitation is that the response can respond in the low-amplitude solution; Sebald et al. (2011) proposed a method to excite the system to jump to the high amplitude solution at low energy cost. Stanton et al. (2010) and Erturk and Inman (2011b) investigated the dynamic response, including the chaotic response, for such a system. Cottone et al. (2009) used an inverted beam with magnets and considered random excitation. Mann and Sims (2009) and Barton et al. (2010) used an electromagnetic harvester with a cubic force non-linearity. Litak et al. (2010) and Ali et al. (2011) investigated non-linear piezomagnetoelastic energy harvesting under random broadband excitation. McInnes et al. (2010) investigated the stochastic resonance phenomena for a non-linear system with a double potential well.

Another requirement of an energy harvester is to harvest reasonable amount of energy when the excitation frequency is low. One example of this is energy harvesting from vibration of long-span bridges and tall buildings. A low-frequency piezoelastic or piezomagnetoelastic harvester is difficult to realise due to small physical dimensions of the devices. In this article, an inverted cantilever beam with piezoelastic patch loaded with a tip mass is investigated. The idea is to adjust the mass, such that the system is near buckling and therefore has a low effective resonance frequency. The beam undergoes large deformations exhibiting a non-linear behaviour, and hence, geometric non-linearities are considered. By exploiting non-linearity, the aim is to have a low-frequency energy harvesting device that is relatively insensitive to a particular excitation frequency and responds with a relatively large amplitude. This article reports theoretical, numerical and experimental investigation of the proposed device.

Inverted beam with tip mass

For non-linear energy harvesting, an inverted elastic beam is considered with a tip mass, and the base is harmonically excited in the transverse direction. In this section, we derive the governing equation of motion using Euler–Bernoulli beam theory. The displacement–curvature relation of the beam is non-linear due to the large transverse displacement of the beam. We assume that the thickness of the beam is small compared with the length, so that the effects of shear deformation and rotary inertia of the beam can be neglected. The beam is such that the first torsional resonance frequency is much higher than the excitation frequency, and the lumped mass is kept symmetric with respect to the centre line. Hence, the vibration is purely planar, and we neglect the torsional modes of the beam in the analysis. These assumptions are consistent with the observations in the laboratory.

Figure 1 shows the beam as a vertical cantilever of length L with harmonic base excitation $z(t) = z_0 \cos \omega t$. The beam carries a concentrated tip mass, M_t, with moment of inertia I_t, at a position L_t from the base of the beam. The horizontal and vertical elastic displacements at the tip mass are v and u, respectively, and s represents the distance along the neutral axis of the beam.

Consider an arbitrary point on the beam, P, at a distance s from the base. This point undergoes a rigid body translation due to the base excitation and a further displacement due to the elastic beam deformation, which is given by $(v_p(s,t), -u_p(s,t))$. Hence, the point P has undergone a total horizontal displacement of $z + v_p$ and a vertical displacement of $-u_p$. Let $\varphi_p(s,t)$ denote the rotation of the beam at s, and hence, the rotation at the tip mass is $\varphi(t) = \varphi_p(L_t, t)$, measured at the mass centre.

In the following analysis, the beam is assumed to have uniform inertia and stiffness properties; a non-

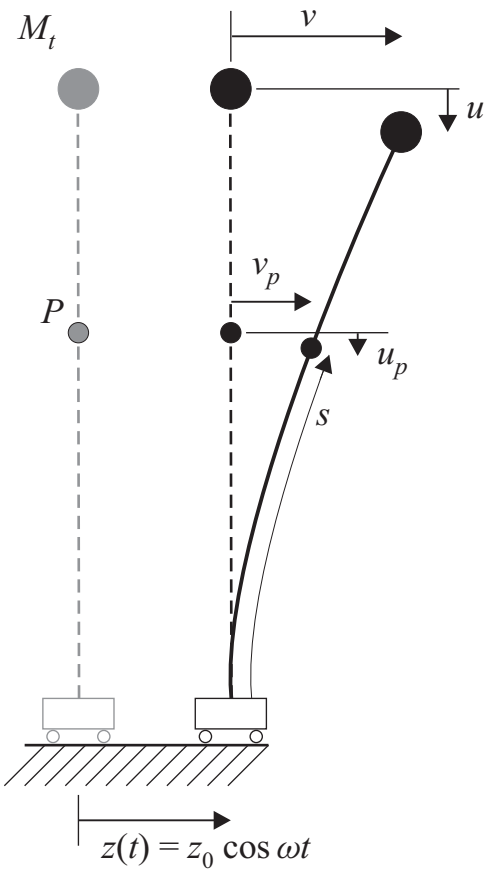

Figure 1. Schematic representation of the inverted beam harvester. M_t denotes the tip mass attached to the elastic beam, while v and u denote the horizontal and vertical displacements of the mass, respectively. Point P denotes an arbitrary point on the beam whose position is described by the coordinates s, v_p and u_p. In this article, piezoelectric patches are placed along the beam but are not shown here.

uniform beam is easily modelled by including the mechanical beam properties in the following energy integrals. The beam has cross-sectional area A, mass density ρ, equivalent Young's modulus E and second moment of area I.

The kinetic energy of the beam-mass system is (Esmailzadeh and Nakhaie-Jazar, 1998)

$$T = \frac{1}{2}\rho A \int_0^L \left[\left(\dot{v}_p(s,t) + \dot{z} \right)^2 + \left(\dot{u}_p(s,t) \right)^2 \right] \mathrm{d}s + \frac{1}{2} M_t \left[(\dot{v} + \dot{z})^2 + \dot{u}^2 \right] + \frac{1}{2} I_t \dot{\phi}^2 \quad (1)$$

where the translation of the tip mass is $v(t) = v_p(L_t, t)$ and $u(t) = u_p(L_t, t)$ and the dot denotes differentiation with respect to time. Equation (1) is obtained by neglecting the effect of rotary inertia of the beam mass.

The potential energy of the system is

$$\Pi = \frac{1}{2} EI \int_0^L (\kappa(s,t))^2 \mathrm{d}s - \rho A g \int_0^L u_p(s,t) \mathrm{d}s - M_t g u \quad (2)$$

where the curvature is (Ali and Padhi, 2009; Nayfeh and Pai, 2004; Zavodney and Nayfeh, 1989)

$$\kappa(s,t) = \frac{\partial \phi_p}{\partial s} = \phi'_p \quad (3)$$

where the prime denotes differentiation with respect to s and g is the gravitational constant. The slope of the beam, ϕ_p, may be written in terms of the beam elastic displacement as

$$\cos \phi_p = 1 - u'_p \text{ or } \sin \phi_p = v'_p \quad (4)$$

Hence (Ali and Padhi, 2009; Nayfeh and Pai, 2004)

$$u'_p = 1 - \sqrt{1 - {v'_p}^2} \approx \frac{1}{2} {v'_p}^2$$

$$\text{or} \quad u_p(s,t) = \frac{1}{2} \int_0^s (v'_p(\xi,t))^2 \mathrm{d}\xi \quad (5)$$

The second of equation (4) gives

$$\phi_p(s,t) = \sin^{-1} v'_p \approx v'_p + \frac{1}{6} {v'_p}^3 \quad (6)$$

and differentiating this equation gives

$$\kappa(s,t) = \phi'_p = \frac{v''_p}{\cos \phi_p} = \frac{v''_p}{\sqrt{1 - {v'_p}^2}} \approx v''_p \left(1 + \frac{1}{2} {v'_p}^2 \right) \quad (7)$$

Equations (5) to (7) have been expanded as Taylor series, and the terms in $O(v_p^4)$ and higher orders are neglected.

In this article, we assume that the tip mass is significantly larger than the beam mass, and hence, a single-mode approximation of the beam deformation is sufficient. The displacement at any point in the beam is represented as a function of the tip mass displacement through a function for the beam deformation, $\psi(s)$, as

$$v_p(s,t) = v_p(L_t, t)\psi(s) = v(t)\psi(s) \quad (8)$$

The displacement may be approximated by any function satisfying the boundary conditions at $s = 0$, for example (Esmailzadeh and Nakhaie-Jazar, 1998)

$$\psi(s) = \lambda_t \left(1 - \cos\left(\frac{\pi s}{2L} \right) \right) \quad (9)$$

where λ_t is a constant, such that $\psi(L_t) = 1$, that is, $\lambda_t = 1/(1 - \cos(\pi L_t / 2L))$. Similar results are obtained

using other displacement models, such as the static beam deflection. The implications of this assumption for the experimental validation will be discussed later.

Using this single-mode approximation, the kinetic and potential energies of the system in terms of the transverse displacement of the tip mass, v, are

$$\begin{aligned} T &= \frac{1}{2}\rho A\int_0^L\left[(\dot{v}\psi(s)+\dot{z})^2+\left(v\dot{v}\int_0^s(\psi'(\xi))^2\mathrm{d}\xi\right)^2\right]\mathrm{d}s \\ &\quad+\frac{1}{2}M_t\left[(\dot{v}+\dot{z})^2+\left(v\dot{v}\int_0^{L_t}(\psi'(s))^2\mathrm{d}s\right)^2\right] \\ &\quad+\frac{1}{2}I_t\left[\dot{v}\psi'(L_t)+\frac{1}{2}v^2\dot{v}(\psi'(L_t))^3\right]^2 \qquad (10) \\ &= \frac{1}{2}\rho A\left[N_1\dot{v}^2+2N_2\dot{v}\dot{z}+\dot{z}^2L+N_3(v\dot{v})^2\right] \\ &\quad+\frac{1}{2}M_t\left[(\dot{v}+\dot{z})^2+N_4^2(v\dot{v})^2\right] \\ &\quad+\frac{1}{2}I_t\left[N_5\dot{v}+\frac{1}{2}N_5^3v^2\dot{v}\right]^2 \qquad (11) \end{aligned}$$

and

$$\begin{aligned} \Pi &= \frac{1}{2}EI\int_0^L\left[v\psi(s)''+\frac{1}{2}v^3(\psi'(s))^2\psi''(s)\right]^2\mathrm{d}s \\ &\quad-\frac{1}{2}\rho Agv^2\int_0^L\left[\int_0^s(\psi'(\xi))^2\mathrm{d}\xi\right]\mathrm{d}s \\ &\quad-\frac{1}{2}M_tgv^2\int_0^{L_t}(\psi'(s))^2\mathrm{d}s \qquad (12) \\ &= \frac{1}{2}EI\left[N_6v^2+N_7v^4+\frac{1}{4}N_8v^6\right] \\ &\quad-\frac{1}{2}N_9\rho Agv^2-\frac{1}{2}N_4M_tgv^2 \qquad (13) \end{aligned}$$

Using the displacement model in equation (9), the constants from N_1 to N_9 are given by

$$\begin{aligned} N_1 &= \int_0^L(\psi(s))^2\mathrm{d}s=\lambda_t^2\left(\frac{3\pi-8}{2\pi}\right)L \\ N_2 &= \int_0^L\psi(s)\mathrm{d}s=\lambda_t\left(\frac{\pi-2}{\pi}\right)L \\ N_3 &= \int_0^L\left(\int_0^s(\psi'(\xi))^2\mathrm{d}\xi\right)^2\mathrm{d}s=\lambda_t^2\left(\frac{\pi^2(2\pi^2-9)}{384}\right)\frac{1}{L} \\ N_4 &= \int_0^{L_t}(\psi'(s))^2\mathrm{d}s=\lambda_t^2\left(\frac{\pi^2}{8}\right)\frac{1}{L_t} \\ N_5 &= \psi'(L_t)=\lambda_t\left(\frac{\pi}{2}\right)\frac{1}{L_t} \\ N_6 &= \int_0^L(\psi''(s))^2\mathrm{d}s=\lambda_t^2\left(\frac{\pi^4}{32}\right)\frac{1}{L^3} \\ N_7 &= \int_0^L(\psi'(s)\psi''(s))^2\mathrm{d}s=\lambda_t^4\left(\frac{\pi^6}{2^9}\right)\frac{1}{L^5} \\ N_8 &= \int_0^L(\psi'(s))^4(\psi''(s))^2\mathrm{d}s=\lambda_t^6\left(\frac{\pi^8}{4096}\right)\frac{1}{L^7} \\ N_9 &= \int_0^L\left[\int_0^s(\psi'(\xi))^2\mathrm{d}\xi\right]\mathrm{d}s=\lambda_t^2\left(-\frac{1}{4}+\frac{1}{16}\pi^2\right) \end{aligned} \qquad (14)$$

Different displacement models will lead to different constants from N_1 to N_9, which may be easily derived using the displacement function $\psi(s)$.

The equation of motion of the beam-mass system is derived in terms of the displacement of the tip mass using Lagrange's equations as

$$\begin{aligned} &\left[N_5^2I_t+M_t+\rho AN_1+\left(\rho AN_3+M_tN_4^2+N_5^4I_t\right)v^2\right]\ddot{v} \\ &+\left[\rho AN_3+M_tN_4^2+N_5^4I_t\right]v\dot{v}^2 \\ &+\left[EIN_6-N_9\rho Ag-N_4M_tg+2EIN_7v^2\right]v \\ &=-\left[\rho AN_2+M_t\right]\ddot{z} \end{aligned} \qquad (15)$$

Damping may also be added to these equations of motion, for example, viscous, material or aerodynamic damping.

Equilibrium positions

The equilibrium positions with no forcing are obtained by setting the velocity and acceleration terms to zero in equation (15) to give

$$\left[EIN_6-N_9\rho Ag-N_4M_tg+2EIN_7v^2\right]v=0 \qquad (16)$$

This equation has either one or three solutions, and $v=0$ is always a solution. Since $N_4>0$, there are three solutions if

$$M_t>\frac{EIN_6-N_9\rho Ag}{N_4g}=M_{tb} \qquad (17)$$

where M_{tb} is the tip mass so that the beam is about to buckle. If the beam mass is neglected, this gives the Euler buckling load as

$$M_{tb}g = \frac{EIN_6}{N_4} = \frac{EI\pi^2}{4L^2} \tag{18}$$

If equation (17) is satisfied, then the non-zero equilibrium positions are given by

$$v_{0b} = \pm\sqrt{\frac{N_9\rho Ag + N_4M_tg - EIN_6}{2EIN_7}} \tag{19}$$

For perturbations about the equilibrium solution at $v = 0$, the linearised equation of motion for the free response is

$$\left[N_5^2I_t + M_t + \rho AN_1\right]\ddot{v} + \left[EIN_6 - N_9\rho Ag - N_4M_tg\right]v = 0 \tag{20}$$

showing that the $v = 0$ equilibrium position is unstable after buckling ($M_t > M_{tb}$) and that before buckling ($M_t < M_{tb}$) the natural frequency for small vibrations is given by

$$\omega_n^2 = \frac{EIN_6 - N_9\rho Ag - N_4M_tg}{N_5^2I_t + M_t + \rho AN_1} \tag{21}$$

After buckling the linearised equation of motion about the equilibrium position v_{0b} becomes, using equation (19)

$$\left[N_5^2I_t + M_t + \rho AN_1 + \left(\rho AN_3 + M_tN_4^2 + N_5^4I_t\right)v_{0b}^2\right]\ddot{\eta} + 4EIN_7v_{0b}^2\eta = 0 \tag{19}$$

where $v = v_{0b} + \eta$. Hence, the natural frequencies about both buckled equilibrium positions are

$$\omega_{nb}^2 = \frac{4EIN_7v_0^2}{N_5^2I_t + M_t + \rho AN_1 + \left(\rho AN_3 + M_tN_4^2 + N_5^4I_t\right)v_{0b}^2} \tag{23}$$

Coupled electromechanical model

There has been a significant modelling effort of piezoelectric materials as distributed transducers and many review articles have been published (see, for example, Benjeddou, 2000; Chee et al., 1998; Chopra, 2002; Crawley, 1994; Leo, 2007). The analyses range from simple devices such as uniform beams and plates in linear dynamics to more complicated configurations such as composites under non-linear and non-uniform loading and dynamics (such as helicopter blades and aircraft wings). A majority of the research deals with the modelling of symmetric (bimorph) beams and plates; however, this article will also consider asymmetric (unimorph) beams. The symmetric device theoretically produces only bending strains; in contrast, the asymmetric device has bending–extension coupling. There are two popular sets of assumptions for modelling strain-induced actuation and sensing. First, the uniform strain model assumes that the through-the-thickness variation of strain in the active piezoelectric device is uniform. This assumption holds true for cases where the passive substrate material is relatively thick compared to the active material. The second case allows for the linear variation of strain in the active material and follows the assumptions of the Euler–Bernoulli model. Crawley and De Luis (1987) and Crawley and Anderson (1990) gave the uniform strain and Euler–Bernoulli derivations for strain-induced actuation. They demonstrated several important results such as the increased effectiveness of the induced-strain actuators for stiffer and thinner bonding layers. Erturk and Inman (2011a) and Leo (2007) give further details of the modelling of piezoelectric sensors and actuators integrated with the beam structures.

Suppose that piezoelectric layers added to a beam in either a unimorph or a bimorph configuration. Then the moment about the beam neutral axis produced by a voltage V across the piezoelectric layers (Crawley and Anderson, 1990; Crawley and De Luis, 1987) may be written as

$$M_\Lambda(s,t) = \gamma_cV(t) \tag{24}$$

where the constant γ_c depends on the geometry, configuration and piezoelectric device.

Hence, for a bimorph with piezoelectric layers in the 31 configuration, with thickness h_c, width b_c and connected in parallel

$$\gamma_c = Ed_{31}b_c(h + h_c) \tag{25}$$

where h is the thickness of the beam and d_{31} is the piezoelectric constant. For a unimorph, the constant is

$$\gamma_c = Ed_{31}b_c\left(h + \frac{h_c}{2} - \bar{z}\right) \tag{26}$$

where $\bar{z}$ is the effective neutral axis (Park et al., 1996). These expressions assume a monolithic piezoceramic actuator perfectly bonded to the beam; Bilgen et al. (2010) considered the effect of the structure of a Macro-Fiber Composite (MFC) on the coupling coefficient and the effect of the bond and Kapton layers. The mechanical stiffness and mass density of the piezoelectric layers should also be included in the beam constants already derived.

The work done by the piezoelectric patches in moving or extracting the electrical charge is

$$W = \int_0^{L_c} M_\Lambda(s,t)\kappa(s)\mathrm{d}s \tag{27}$$

where L_c is the active length of the piezoelectric material, which is assumed to be attached at the clamped end of the beam. Using the approximation for κ in

equation (7), and the displacement model in equation (8), we have

$$W \approx \left(\Theta_1 v + \frac{1}{3}\Theta_2 v^3\right) V \tag{28}$$

where

$$\Theta_1 = \gamma_c \int_0^{L_c} \psi''(s)\mathrm{d}s = \gamma_c \psi'(L_c) \tag{29}$$

and

$$\Theta_2 = 3\gamma_c \int_0^{L_c} \frac{1}{2}\psi''(s)(\psi'(s))^2\mathrm{d}s = \frac{1}{2}\gamma_c(\psi'(L_c))^3 \tag{30}$$

Equation (28) results in additional terms in the mechanical equation of motion, which becomes

$$\begin{aligned}&\left[N_5^2 I_t + M_t + \rho A N_1 + \left(\rho A N_3 + M_t N_4^2 + N_5^4 I_t\right) v^2\right]\ddot{v} \\ &+ \left[\rho A N_3 + M_t N_4^2 + N_5^4 I_t\right] v\,\dot{v}^2 \\ &+ \left[EIN_6 - N_9 \rho A g - N_4 M_t g + 2EIN_7 v^2\right] v \\ &- \Theta_1 V - \Theta_2 v^2 V = -\left[\rho A N_2 + M_t\right]\ddot{z}\end{aligned} \tag{31}$$

On the electrical side, the piezoelectric patches may be considered as a capacitor, and the charge they produce is given by $\Theta_1 v + \Theta_2 v^3$, where Θ_1 and Θ_2 are given by equations (29) and (30), respectively. The electrical circuit considered is represented by a resistive shunt connected across the piezoelectric patch. The electrical equation then becomes

$$C_p \dot{V} + \frac{V}{R_l} + \Theta_1 \dot{v} + \Theta_2 v^2 \dot{v} = 0 \tag{32}$$

where R_l is the load resistor and C_p is the capacitance of the piezoelectric patch.

The average power scavenged between times T_1 and T_2 is calculated as

$$P_{ave} = \frac{1}{T_2 - T_1}\int_{T_1}^{T_2} \frac{V(t)^2}{R_l}\mathrm{d}t \tag{33}$$

Table 1. Parameter values used in the simulation.

Beam and tip mass		Energy harvester	
ρ	7850 kg/m^3	L_c	28 mm
E	210 GN/m^2	b_c	14 mm
b	16 mm	h_c	300 μm
h	0.254 mm	γ_c	-4.00×10^{-5} Nm/V
$L = L_t$	300 mm	C_p	51.4 nF
I_t/M_t	40.87 mm^2	R_l	$10^5 - 10^8\,\Omega$

Numerical simulations

The parameters considered for the numerical simulations are given in Table 1. The beam-mass system is excited at the base with harmonic excitation. Note that when the tip mass is changed, the ratio of M_t/I_t is maintained; this is equivalent to increasing the tip mass width to increase the tip mass.

Figure 2(a) shows the equilibrium position of the tip mass, using the analysis described in section 'Equilibrium positions', and shows that the post-buckled response has two equilibrium positions. Figure 2(b) shows the corresponding natural frequency of the linearised system with the change in the tip mass; both the pre-buckled and post-buckled natural frequencies are given. Linearisation about both equilibrium positions provides the same natural frequencies as the system is assumed to be symmetric. Figure 2(b) shows that the natural frequency of the inverted elastic pendulum decreases with increasing tip mass and is zero at the Euler buckling load corresponding to an estimated tip mass of 10.0 g. Further increases in tip mass cause the beam to buckle, and the natural frequencies about the stable equilibrium positions increase with the tip mass. Thus, the inverted elastic beam-mass system is able to resonate at low frequencies close to the buckling condition. The post-buckled equilibrium positions are quite

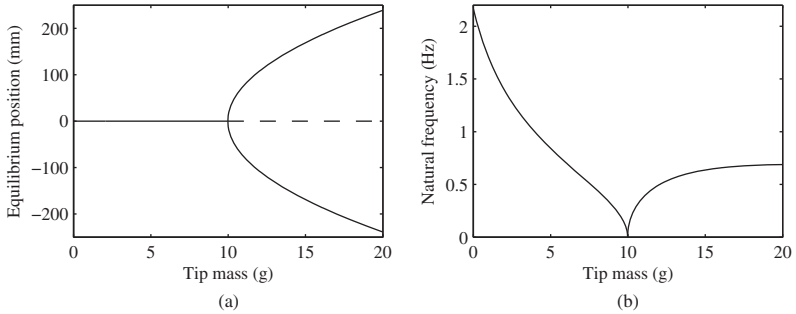

Figure 2. The effect of the tip mass on (a) the equilibrium position and (b) the corresponding natural frequencies for the stable equilibrium positions. The dashed line denotes unstable equilibrium positions.

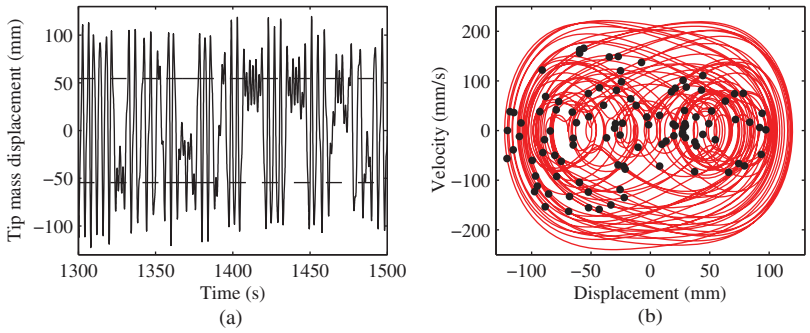

Figure 3. Harvester non-periodic response for the parameters given in Table 1 and a harmonic excitation with $z_0 = 16$ mm at frequency 0.5 Hz: (a) displacement time history and (b) phase portrait for the tip mass. The dashed horizontal lines in (a) show the equilibrium positions of the tip mass. The dots in (b) represent the Poincaré points. The response was obtained using zero initial conditions for the tip mass displacement and velocity.

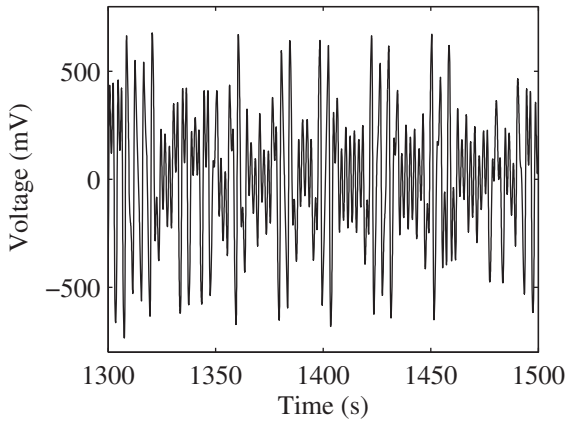

Figure 4. Time history of the voltage across the piezoelectric layers with the parameters given in Table 1 and corresponding to the response given in Figure 3.

sensitive to the tip mass, and in the simulation study, a tip mass of 10.5 g was used, unless stated otherwise.

Figure 3 shows the time history of the tip displacement and the phase portrait of the inverted beam energy harvester system with the parameters given in Table 1 and with zero initial displacement and velocity. The response is only shown from $t = 1300$ s to $t = 1500$ s to demonstrate the characteristics of the beam dynamics. In particular, the beam response sometimes oscillates around one of the equilibrium positions and sometimes exhibits large oscillations either side of the unstable zero displacement position. The corresponding voltage across the piezoelectric layer is shown in Figure 4. Figures 3(a) and 4 show that when the tip mass oscillates close to one of the equilibrium positions, then the voltage across the piezoelectric layer (and therefore the power scavenged) is less than when the tip mass moves back and forth between the potential wells.

The value of the tip mass is now swept from 8 to 20 g. The time response is simulated, with zero initial displacement and velocity, for 8000 cycles to ensure that the transient dynamics have decayed. For the last 100 cycles, the Poincaré points are sampled, and the points corresponding to the displacement response of the tip mass are shown in Figure 5(a) as a bifurcation diagram (Nayfeh and Mook, 1979). The bifurcation diagram is complex and shows periodic solutions at the excitation frequency (a single dot) at some values of tip mass, periodic responses with a period larger than that of the excitation (multiple dots) and chaotic responses (solid blocks of dots). Examples of these responses will be shown later. For the highly buckled case (for large tip masses), the solution is often periodic although the character of the solutions changes abruptly as the tip mass changes. For these cases, there are likely to be multiple coexisting solutions, and the solutions obtained in the bifurcation diagram arise from the initial conditions chosen. The asymmetry in the response about the vertical beam position arises because of the phasing of the forcing, which determines the times when the Poincaré points are sampled. A discontinuity is seen at $M_t = 8.8$ g, which corresponds to the jump in the resonance due to the hardening stiffness characteristic. This looks different from the standard jump phenomena because here the resonance frequency is varied while keeping the excitation frequency fixed; normally, the excitation is changed for a fixed system.

Figure 5(b) shows the average power scavenged by the piezoelectric patches, and this also shows a peak at $M_t = 8.8$ g due to the resonance. The power scavenged at other values of the tip mass in the pre-buckled case is very low. The average power scavenged in the post-buckled regime shows various trends that highlight the existence of multiple coexisting solutions. This is shown most clearly at higher values of tip mass where low-energy solutions exist where the beam response is solely within one potential well and high-energy solutions exist where the beam response oscillates between both potential wells. For tip masses just higher than the buckling mass, the response may be either periodic or

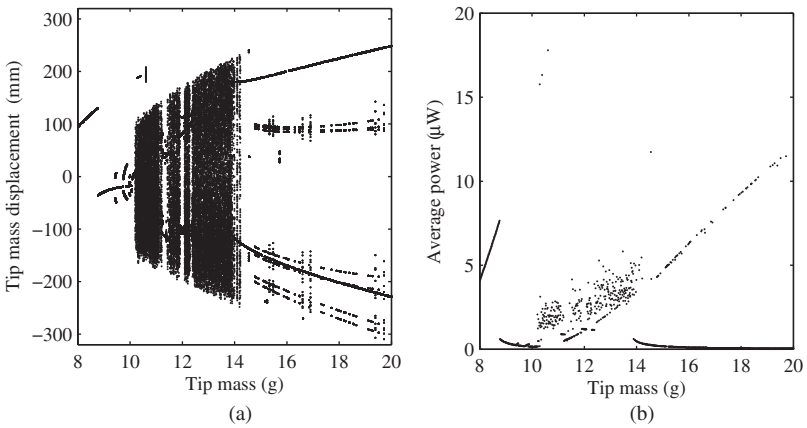

Figure 5. The effect of the variation of the tip mass for a base excitation of $z_0 = 16$ mm at frequency 0.5 Hz and for a load resistance $R_l = 100\,\text{k}\Omega$: (a) bifurcation diagram and (b) average harvested power. The results were obtained using zero initial conditions for the tip mass displacement and velocity.

chaotic, and the chaotic response often gives a slightly higher average power output.

The response dynamics is further investigated in Figure 6 through the detailed analysis of time responses for typical tip mass values. Figure 6(a) shows period 1 response at the pre-buckled resonance. Figure 6(b) also shows a period 1 response, but the beam is in the post-buckled regime where most of the responses are chaotic and produce lower power output. An example of the chaotic response is given in Figure 6(c). Figure 6(d) shows the response for the highest average output power, which shows some chaotic response superimposed on a period 1 response. Examples of low- and high-power solutions for large values of tip mass are shown in Figure 6(e) and (f). The low power response oscillates in one of the potential wells, whereas the high-power response is a period 7 response crossing back and forth between the potential wells. It should be emphasised that other solutions also exist for other values of tip mass, for example, period 3 or period 5 solutions.

Figure 7 shows a parametric study varying the resistance across the piezoelectric layer. Figure 7(a) shows a bifurcation diagram and highlights that periodic responses are seen at high resistance. Figure 7(b) shows the corresponding average power output and shows a clear peak for the period 3 oscillations close to $R_l = 10\,\text{M}\Omega$. This optimum load resistance is very high because of the low capacitance of the piezoelectric layers and because the excitation frequency is very low.

The effect of the base excitation amplitude and frequency is shown in Figures 8 and 9, respectively. At low excitation amplitudes, the beam mass vibrates within one of the potential wells, and the power available is very low. As the excitation amplitude is increased, the tip mass starts jumping from one potential well to the other, which increases the power harvested from the system. For higher excitation amplitudes, the response can be either chaotic or periodic, and the periodic solutions with motion across both the potential wells have a higher power output. At very high excitation amplitudes, the response is period 1, and this gives a higher power output.

For excitation frequencies up to about 0.5 Hz, the response is predominantly periodic with an increasing response amplitude and corresponding power output. For higher frequencies, the response becomes chaotic, before becoming periodic (with various periods) for frequencies above about 0.56 Hz. The power output in Figure 9(b) shows that the responses have different characteristics, and again, multiple coexisting solutions are likely to occur for these excitation frequencies.

Experimental testing

An experimental system was built to validate the model and to determine the effects of unmodelled non-linearities (e.g. piezoelectric hysteresis, noise in the base excitation and out-of-plane motion). As shown in the model earlier, the main parameters of interest are the tip mass, the load resistance and the base excitation amplitude and frequency. The response of the beam is characterised by its transverse displacement and power output through a resistive shunt. A load resistor is used to characterise the energy harvesting performance instead of other passive or active circuits; therefore, the analysis is focused on the fundamental non-linear dynamic behaviour of the cantilever energy harvester.

A National Instruments (NI) cDAQ 9172 data acquisition system, controlled with a code written in LabVIEW software, was employed to automatically examine the mechanical and electrical responses of the inverted cantilever piezocomposite beam. For each experiment, a tip mass, constructed using several magnets, was selected and attached to the beam manually. A load resistor was then selected using an

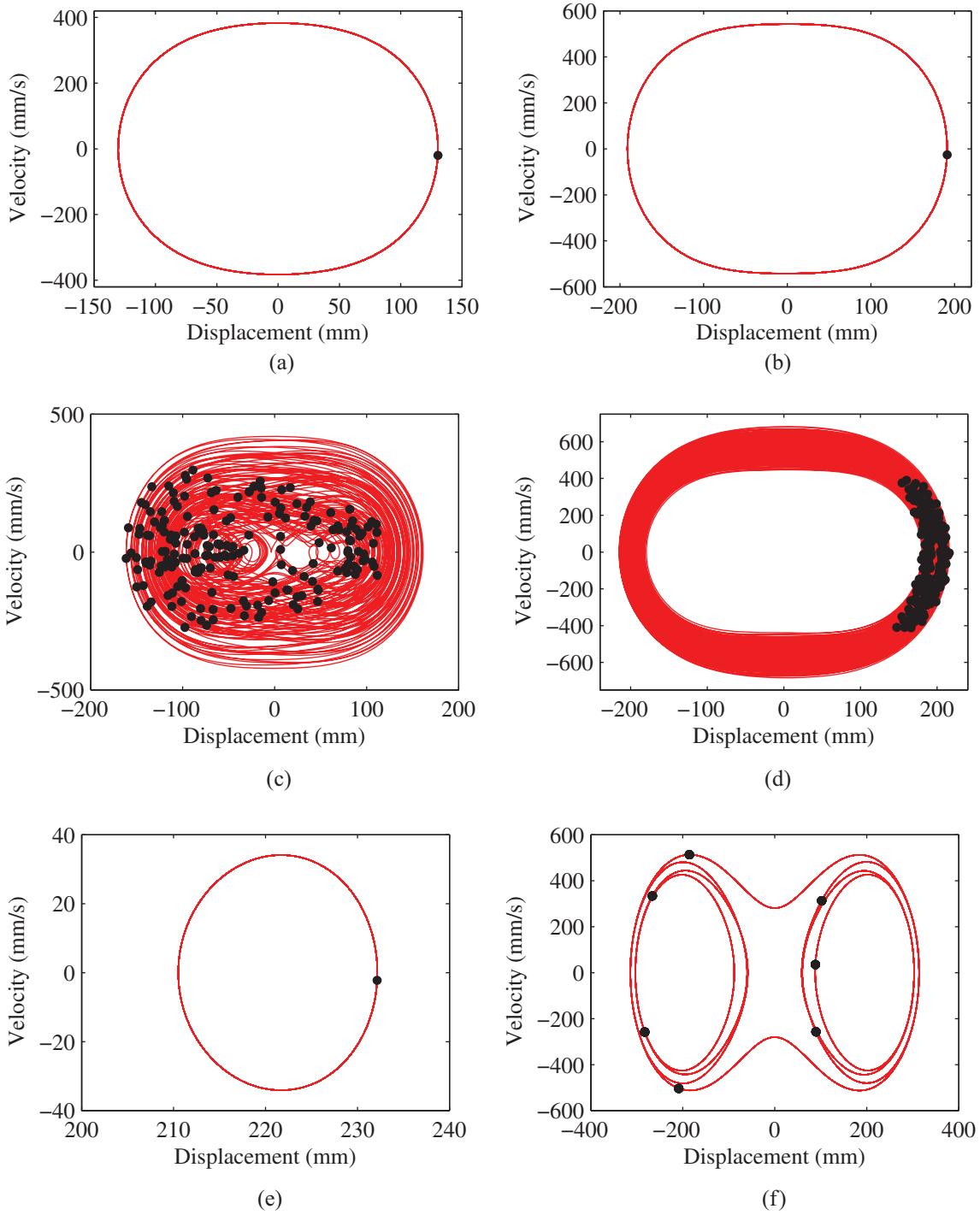

Figure 6. Phase portraits of the tip mass response for a base excitation of $z_0 = 16$ mm at frequency 0.5 Hz and for a load resistance $R_l = 100\,\text{k}\Omega$: (a) $M_t = 8.76$ g, $P_{ave} = 7.65\,\mu$W, (b) $M_t = 10.39$ g, $P_{ave} = 16.3\,\mu$W, (c) $M_t = 10.5$ g, $P_{ave} = 2.40\,\mu$W, (d) $M_t = 10.61$ g, $P_{ave} = 17.8\,\mu$W, (e) $M_t = 18.6$ g, $P_{ave} = 0.056\,\mu$W and (f) $M_t = 18.65$ g, $P_{ave} = 10.2\,\mu$W. The dots represent the Poincaré points. The results were obtained using zero initial conditions for the tip mass displacement and velocity.

electromagnetic relay circuit, and the base displacement peak amplitude was chosen. The frequency of excitation was then swept in both increasing and decreasing directions. This process was repeated for all of the selected parameters.

The beam was excited for 30 complete cycles (of base excitation) for each combination of parameters in order to minimise the effect of transient motion. Only the last 10 cycles were recorded and analysed. Since the frequency was incremented in small steps and the waveform was continuous between each frequency, the disturbance (e.g. rapid accelerations) to the beam was minimised. This is important since such disturbances will result in a premature transition to an alternative

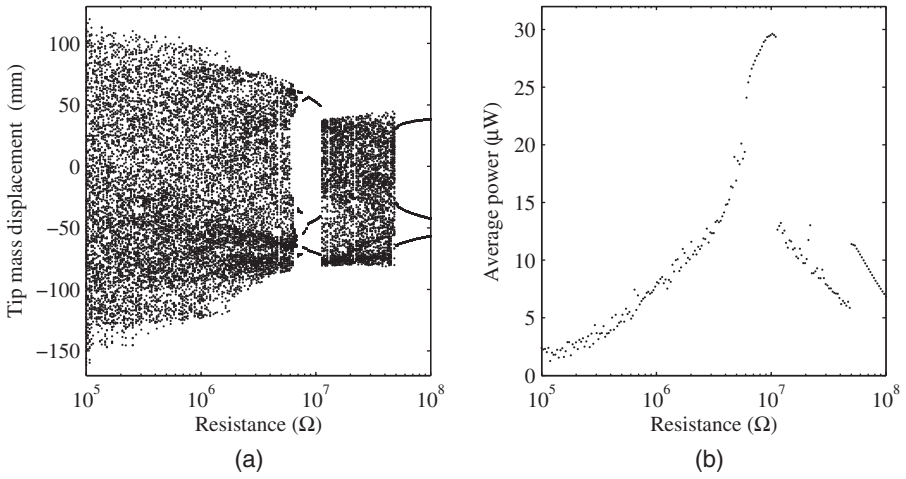

Figure 7. The effect of the resistance across the piezoelectric layer, for a tip mass of $M_t = 10.5$ g and a base excitation of amplitude $z_0 = 16$ mm at frequency $\omega = 0.5$ Hz: (a) bifurcation diagram and (b) average harvested power. The results were obtained using zero initial conditions for the tip mass displacement and velocity.

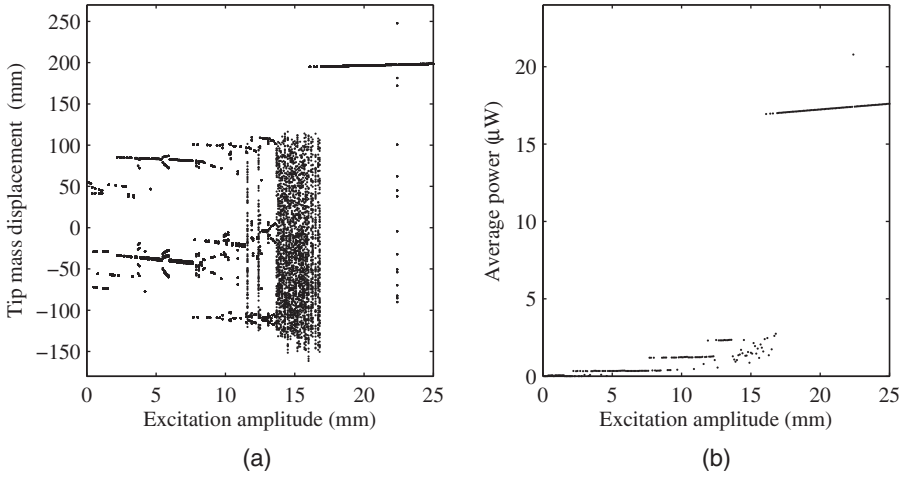

Figure 8. The effect of the amplitude of the base excitation at an excitation frequency of 0.5 Hz, a tip mass of $M_t = 10.5$ g and a load resistance $R_l = 100$ kΩ: (a) bifurcation diagram and (b) average harvested power. The results were obtained using zero initial conditions for the tip mass displacement and velocity.

solution as the frequency is increased and decreased. Although most ambient sources of vibration will be multi-tone and have noise, the current research concentrates on single-tone excitations.

The control signal for the base excitation was produced by an NI 9263 cDAQ module with 16 bit resolution (set to ±10 V range) at a generation rate of 10 kHz. This control signal was low-pass (LP) filtered using a Kemo (type VBF/24) elliptic filter with a 5-Hz cut-off frequency to minimise the high-frequency noise from the digital-to-analog converter (DAC). Note that the filtered output of the DAC was not measured as the reference signal; therefore, the lag effect of the filter was avoided. The base excitation signal was connected to a Bytronic Pendulum Control System, consisted of a belt-driven linear slider that moves on a track and is actuated by a direct current (DC) motor. A multi-turn potentiometer monitors the position of the belt and hence the position of the linear slider. A displacement feedback controller ensures that the displacement is proportional to the control signal. The linear slider has low inertia and that there is no return spring (as in an electromagnetic shaker). The fact that the slider has low inertia means that the base motion is affected by small imperfections in the linear track. In addition, since the system is driven by the forcing of the DC motor only (e.g. no return spring), the actual excitation deviates from the desired harmonic excitation near the $\dot{z} = 0$ condition. Both of these deviations are measured by the potentiometer; however, their effects on the general motion and the power output were assumed negligible.

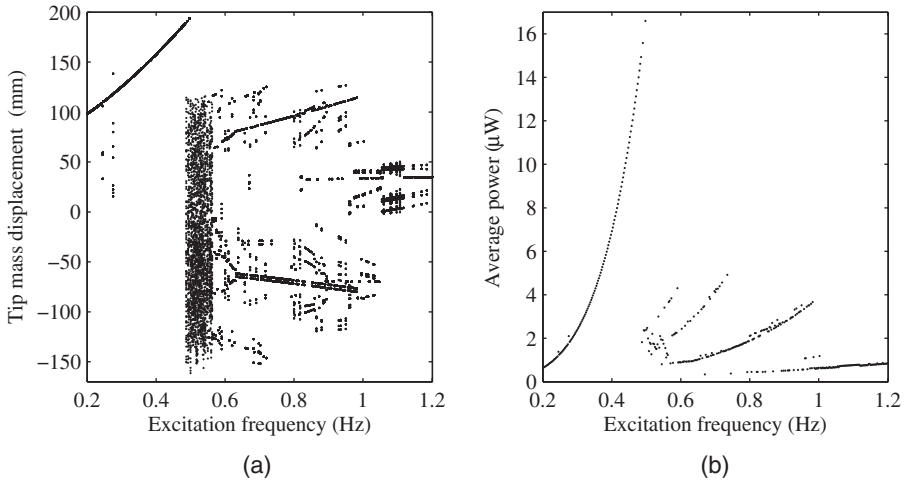

Figure 9. The effect of the frequency of the base excitation for an excitation amplitude of $z_0 = 16$ mm, a tip mass of $M_t = 10.5$ g and a load resistance $R_l = 100\,\text{k}\Omega$: (a) bifurcation diagram and (b) average harvested power. The results were obtained using zero initial conditions for the tip mass displacement and velocity.

A clamping mechanism, which applies uniform pressure across the clamped surface of the beam, was attached to the linear slider. All experiments presented in this article were conducted without removing the beam from the clamp; therefore, consistent boundary conditions were achieved across all cases. A beam made of spring steel of thickness 0.245 mm, width 15.88 mm and free length 293 mm was used as the cantilever. Figure 10 shows the beam mounted on the linear slider.

A single piezocomposite patch, the MFC model M2814-P2 manufactured by Smart Material Corp., of active length 28 mm and active width 14 mm was bonded to the beam near the clamped end in a unimorph configuration. The MFC was developed at the NASA Langley Research Center (Wilkie et al., 2000). An MFC is a flexible, planar actuation device that employs rectangular cross-section, unidirectional piezoceramic fibres (PZT 5A) embedded in a thermosetting polymer matrix (High and Wilkie, 2003). An electromechanical characterisation of the mechanical and piezoelectric behaviour of the MFC device can be found in Bilgen et al. (2012). Since the purpose here is to improve power output, the MFC with through-the-thickness poling (type P2), which operates in the 31 electromechanical mode, was chosen. The 31-mode device has approximately 40 times higher capacitance compared to the interdigitated 33-mode device (type P1). The patch was aligned to the beam symmetrically in the widthwise direction and as close to the base as possible. The MFC was bonded to the beam using a 3M DP460 type two-part epoxy and let for cure under ≈1 atm vacuum.

The tip mass was implemented using several disc-like neodymium magnets with diameter 10 mm, height 5 mm and approximate mass 1.75 g, whose positions could be moved easily. In the model, the mass was assumed to be at the end of the beam; the portion of the beam above the magnets in the experiment has little effect on the system dynamics.

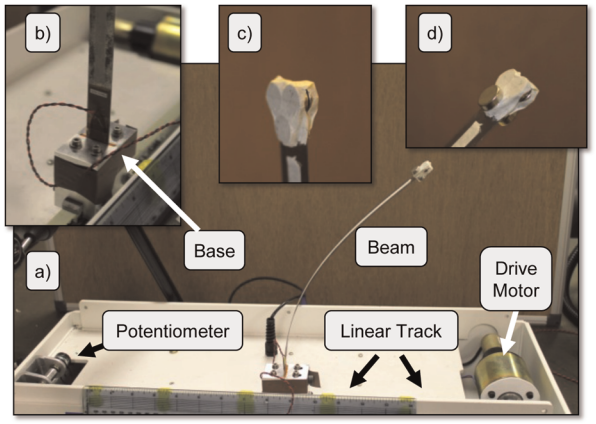

Figure 10. Picture of the experimental set-up. (a) Linear slider and the inverted cantilever beam with 14.0 g tip mass. (b) Base of the beam showing the MFC device. (c) Tip mass of 10.5 g shown nearly vertical at the stable equilibrium. (d) Tip mass of 14.0 g showing approximately 45° end slope in a stable equilibrium. Note that laser displacement sensor is not shown. MFC: Macro-Fiber Composite.

The signals of interest are measured using a NI 9215 analog-to-digital converter (ADC) module with 16 bit resolution (set to ±10 V range) at a variable sample rate. During the acquisition period, 100 points per base excitation cycle were captured. Three signals were measured: the potentiometer output, which is proportional to the base displacement; the laser displacement sensor (MTI LTC-300-200-SA with ±20 μm resolution), which measures the mid-line of the beam at 100 mm from the base; and the voltage output of the MFC piezocomposite device. A 10:1 voltage divider probe

Table 2. Resistor values used in the experiment.

Nominal resistance	Measured resistance at piezo output
10 kΩ	9.91 kΩ
100 kΩ	99.3 kΩ
150 kΩ	146.9 kΩ
330 kΩ	318.3 kΩ
450 kΩ	450.6 kΩ
1 MΩ	910 kΩ
1.5 MΩ	1.658 MΩ
2.2 MΩ	2.272 MΩ
3.3 MΩ	3.344 MΩ
Open	9.944 MΩ

(Agilent N2862A) with equivalent 9.95 MΩ input impedance is used to monitor the voltage output of the piezocomposite device.

As noted earlier, four parameters were varied. The tip mass values were chosen as $M_t = 0$, 10.5 g (six magnets, $L_t = 287$ mm, pre-buckling) and 14 g (eight magnets, $L_t = 284$ mm, post-buckling) representing three fundamentally different dynamic behaviours. A total of 10 load resistance values were applied. Table 2 shows the effective load resistances connected to the MFC device. Note that the probe and ADC input impedances were included in the effective load resistance as well as the selected resistor. The load resistances were measured using an Agilent digital multimeter.

Base displacement peak amplitudes of 5, 10, 15, 20 and 25 mm were utilised. This range was not exceeded due to several reasons, which are artificially introduced by the experimental set-up. First, large beam displacements exceed the measurement range of the laser, although the electrical response could still be measured. Second, the magnets attract and attach to the slider track when high curvatures are present. In addition to the parameters above, the frequency of base excitation was examined in the range 0.3–3 Hz, although the range was adjusted depending on the tip mass.

Experimental results

As noted earlier, three tip mass values are evaluated. In this section, the fundamental response of the vibration energy harvester is evaluated in terms of two quantities: the measured displacement at a single point 100 mm from the base of the beam divided by the base displacement, and the measured power output through the known effective resistance divided by the base displacement squared. It is important to note that the response waveforms are not necessarily a single harmonic; therefore, each waveform is integrated over the time of interest to calculate their average values. The average value of the beam displacement and power output is obtained by integrating the measured values of the waveform over 10 cycles and dividing the integral by the total time. In the case of base displacement, the absolute values are taken before the integration.

Figure 11(a) shows the ratio of the average displacement measured at the laser to the harmonic displacement response at the base of the inverted cantilever beam with no tip mass. As expected, the response is approximately linear, with a natural frequency range of 2.43–2.47 Hz for the base displacement range of 5–20 mm. As the base displacement amplitude is increased, the mechanical output/input ratio decreases and the peak frequency increases. These results are typical for a hardening non-linearity. Figure 11(b) shows the ratio of the average power output to the square of the harmonic

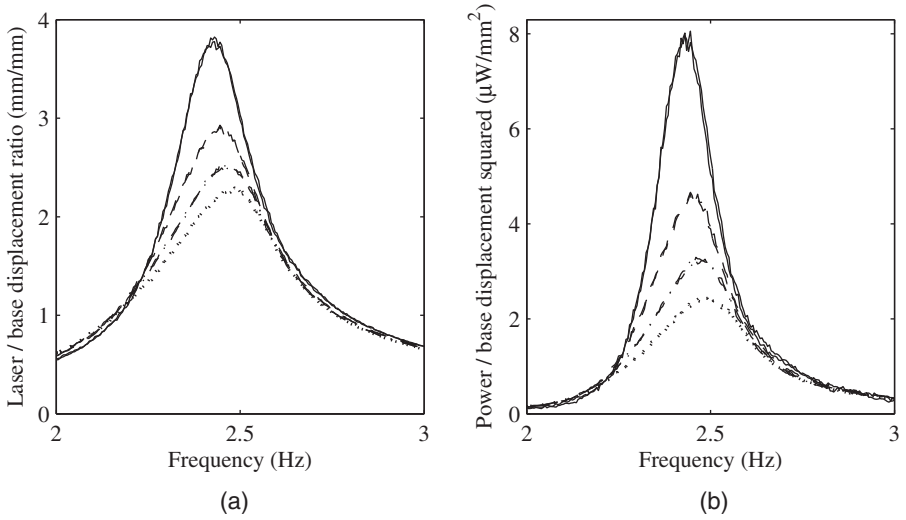

Figure 11. The experimental results for a tip mass of $M_t = 0$ g and a base excitation with amplitudes of $z_0 = 5$ (solid), 10 (dashed), 15 (dash–dot) and 20 mm (dotted) at a range of frequencies: (a) response measured by laser and (b) average harvested power. $R_l = 1.658$ MΩ for all measurements.

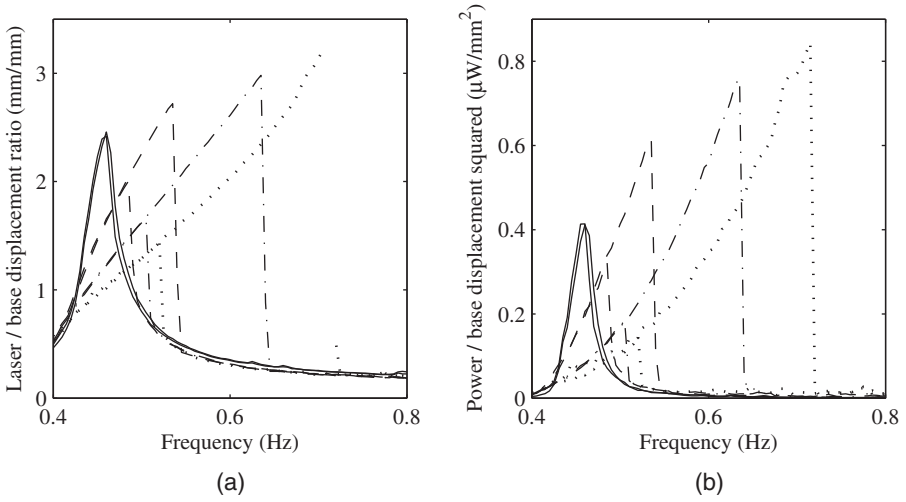

Figure 12. The experimental results for a tip mass of $M_t = 10.5$ g and a base excitation with amplitudes of $z_0 = 5$ (solid), 10 (dashed), 15 (dash–dot) and 20 mm (dotted) at a range of frequencies: (a) response measured by laser and (b) average harvested power. $R_l = 9.944\,\text{M}\Omega$ for $z_0 = 5$ and 10 mm and $R_l = 3.344\,\text{M}\Omega$ for $z_0 = 15$ and 20 mm.

displacement response at the base of the inverted cantilever beam with no tip mass. If the system was linear, then these curves would overlay for different values of base excitation; however, in this case, the ratio reduces as the base displacement amplitude increases.

Figure 12 shows the average displacement and power results for the inverted cantilever beam with a tip mass of 10.5 g. At this value of tip mass, the beam has not buckled, and the simulations show that the maximum power is generated before the beam buckles, close to the resonance. This prediction is consistent with the experimental response when pre-buckled and post-buckled cases are compared. The resonance frequency of the device can be easily tuned by moving the tip mass, and hence, the resonance may be tuned to the harmonic excitation frequency. The responses show the classical jump phenomena for a hardening non-linearity, where the jump down occurs when slowly increasing the excitation frequency and the jump up occurs when reducing the excitation frequency. Thus, there is a range of frequencies where two stable coexisting solutions exist.

Figure 13 shows the effect of varying the load resistance on the maximum power output for the inverted cantilever beam with a tip mass of 10.5 g. For each load resistance and base excitation amplitude, the excitation frequency is swept in both the increasing and the decreasing directions. Since the beam represents a hardening non-linearity, the maximum power occurs during the upward frequency sweep. The maximum power is identified during this sweep and included in Figure 13. There is an optimum load resistance that gives the maximum power (compare to Figure 7(b)), and the optimum resistance value decreases with increasing base excitation amplitude. This is expected as the maximum response occurs at a higher frequency when the

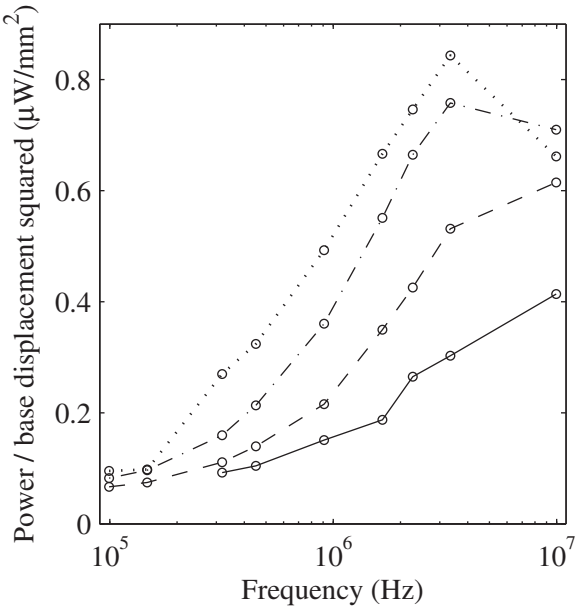

Figure 13. The experimental maximum power for a tip mass of $M_t = 10.5$ g and a base excitation with amplitudes of $z_0 = 5$ (solid), 10 (dashed), 15 (dash-dot) and 20 mm (dotted) for a range of load resistance.

excitation amplitude is increased. The range of load resistance values is very high, because the frequencies of interest are very low. Also, note that the maximum resistance that may be implemented is limited by the ADC input impedance.

Figure 14 shows the average displacement and power results for the inverted cantilever beam with a tip mass of 14 g. At this tip mass value, the beam is buckled, and the dominant mode of vibration is a single-well oscillation. When base displacement amplitude is sufficiently

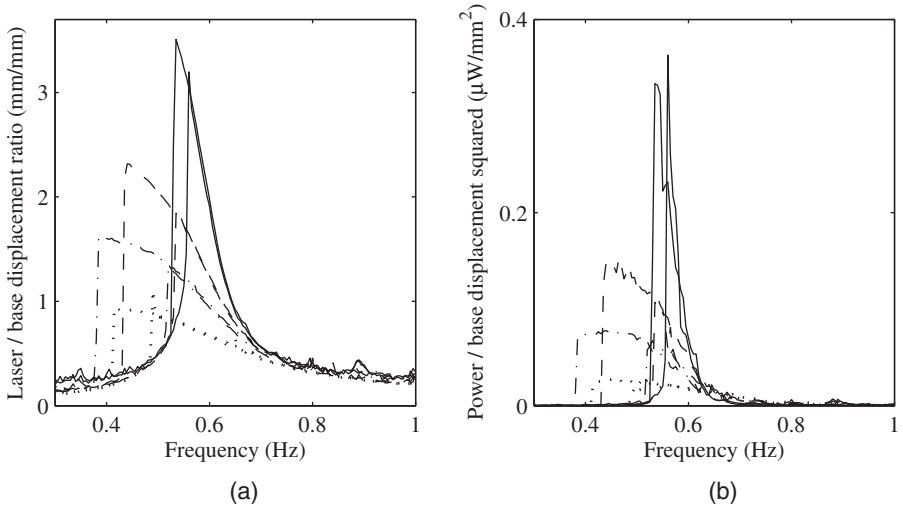

Figure 14. The experimental results for a tip mass of $M_t = 14$ g and a base excitation with amplitudes of $z_0 = 5$ (solid), 10 (dashed), 15 (dash-dot) and 25 mm (dotted) at a range of frequencies: (a) response measured by laser and (b) average harvested power. $R_l = 9.944\,\text{M}\Omega$ for all measurements.

large, or a resonance is excited about a specific stable equilibrium, cross-well oscillations may occur, although none were observed in Figure 14. The power output for the post-buckled configuration is significantly smaller than that for the pre-buckled configuration.

Simulated results

The experimental system was modelled using the equations of motion of the inverted cantilever beam developed earlier in order to validate the model. There are two linked issues with simulating the tested system: the parameters of the model may only be obtained approximately from the geometry of the structure and the material properties, and the response is highly sensitive to some parameters in the model. In addition, damping is very difficult to model and in reality will mainly consist of viscoelastic material damping and air damping. In the model, a linear viscous damper has been included, where the coefficient varies with the response amplitude.

The single piezoelectric patch adds significant stiffness to the beam and will also cause a shift in the neutral axis of the beam. This will also change the mode shapes of the beam and therefore the displacement function if taken as the first mode. Here, we have considered only a very simple model of the beam, where the displacement model is given by equation (9) and the neutral axis is assumed to remain at the centre of steel beam. Using the mechanical properties and geometry of the MFC gives an increase in EI of 100% over and above that for the uniform steel beam, and a corresponding increase in the N_6 and N_7 terms in the equations of motion of 19% and 0.57%, respectively. The electromechanical coupling coefficient is calculated as $\gamma_c = -1.49\times10^{-5}\,\text{Nm/V}$.

The viscous damping coefficient is adjusted for each simulated run to give a similar qualitative response to the measured response. The damping from the air resistance is likely to increase with higher amplitude motion, and hence, the coefficient will increase for high excitation amplitudes. For the cases without the tip mass and when $M_t = 10.5$ g, the viscous damping coefficient was set at 0.0032, 0.0038, 0.0045 and 0.0053 for excitation amplitudes of $z_0 = 5$, 10, 15 and 20 mm, respectively. When $M_t = 14$ g, the coefficient was increased to 0.0048, 0.0057, 0.009 and 0.014 for $z_0 = 5$, 10, 15 and 20 mm, respectively. Note that the simulated displacements are given at the tip mass, whereas the experimental displacements are given at a fixed height determined by the position of the laser sensor.

Figures 15 to 17 show the simulated results corresponding to the measurements given in Figures 11 to 14 and show similar trends to the experimental results. Without a tip mass, Figure 15 shows that the response is approximately linear with the hardening non-linearity slightly increasing the natural frequency and slightly reducing the frequency response function amplitude, as the base excitation amplitude increases. When a tip mass of $M_t = 10.5$ g is added, the simulated results in Figure 16 show the jump phenomena of a hardening non-linearity. The jump frequencies are very sensitive to the damping coefficient and the tip mass (compared to that required for the beam to buckle).

For a tip mass of $M_t = 14$ g, the beam has buckled, and this results in a softening non-linearity with some jumps, with the response located in a single potential well, as shown in Figure 17. In this case, the damping coefficients have had to be increased; with lower damping, at some frequencies, the beam can hop between potential wells, and multiple solutions coexist.

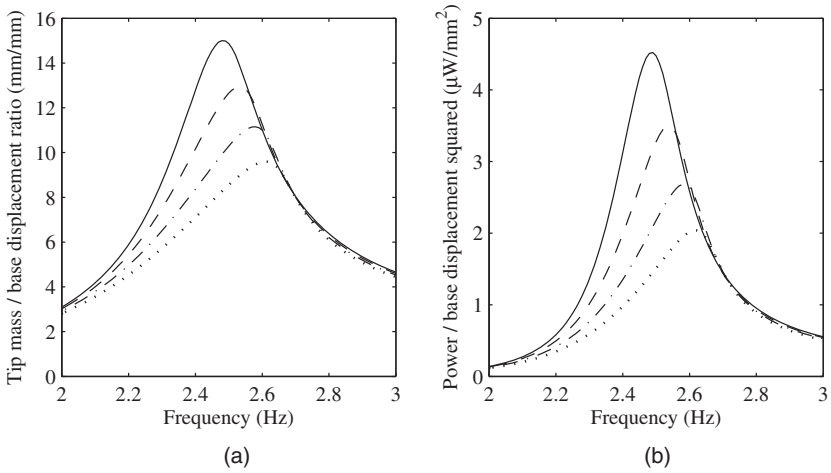

Figure 15. The simulated results for a tip mass of $M_t = 0$ g and a base excitation with amplitudes of $z_0 = 5$ (solid), 10 (dashed), 15 (dash–dot) and 20 mm (dotted) at a range of frequencies: (a) tip mass response and (b) average harvested power. $R_l = 1.658\,\text{M}\Omega$ for all cases.

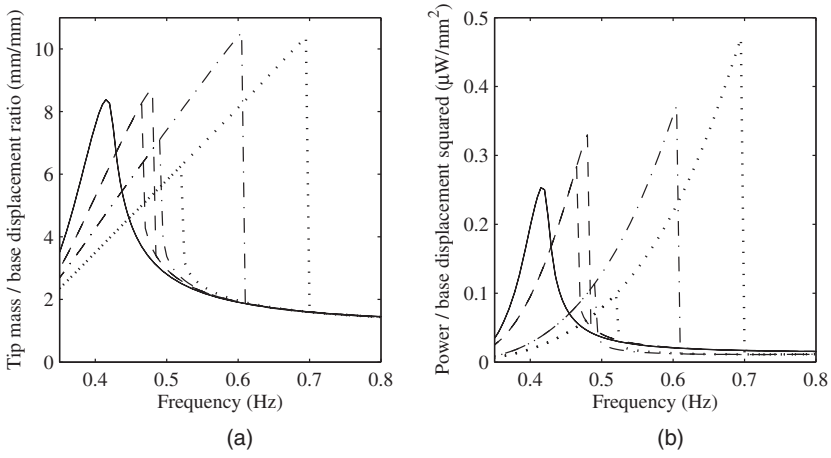

Figure 16. The simulated results for a tip mass of $M_t = 10.5$ g and a base excitation with amplitudes of $z_0 = 5$ (solid), 10 (dashed), 15 (dash–dot) and 20 mm (dotted) at a range of frequencies: (a) tip mass response and (b) average harvested power. $R_l = 9.944\,\text{M}\Omega$ for $z_0 = 5$ and 10 mm and $R_l = 3.344\,\text{M}\Omega$ for $z_0 = 15$ and 20 mm.

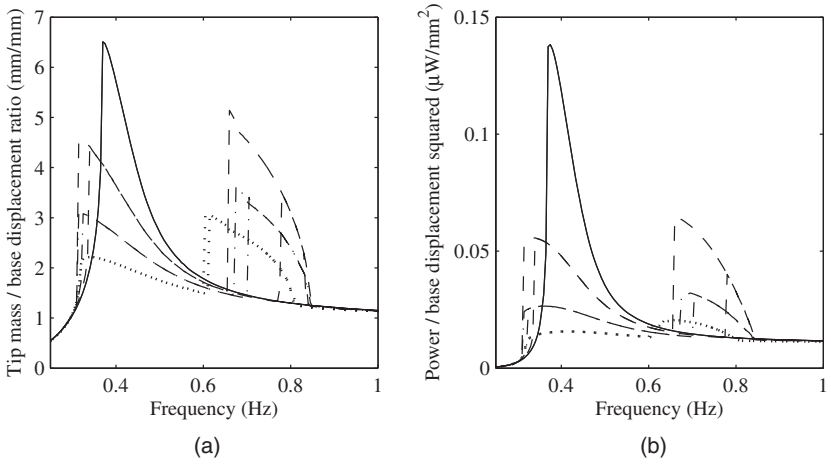

Figure 17. The simulated results for a tip mass of $M_t = 14$ g and a base excitation with amplitudes of $z_0 = 5$ (solid), 10 (dashed), 15 (dash-dot) and 20 mm (dotted) at a range of frequencies: (a) tip mass response and (b) average harvested power. $R_l = 9.944\,\text{M}\Omega$ for all cases.

Subharmonic resonances are also clear in the simulated results, and the resonance at twice the primary resonance frequency is readily identified. Subharmonic resonances are not apparent on the experimental results although there is some increase in amplitude at these higher frequencies. The power generated in this simulated case is also very low because the response stays completely within in a single potential well. The equilibrium configuration and the dynamic response are very sensitive to all of the inertia and stiffness parameters in the equations of motion, in addition to the damping properties, and this makes a quantitative comparison with the experimental results difficult.

Conclusion

The proposed energy harvesting system addresses a very difficult problem where energy is required from a structure with low excitation frequency and high displacement, such as a highway bridge. A resonant linear harvester based on a cantilever beam is difficult to implement because the low natural frequency requires a very large or a very flexible beam. In this article, a low-frequency piezoelectric energy harvester is proposed using an inverted elastic beam-mass system. The equations of motion for the proposed system were developed, the response was simulated and this model was validated experimentally. The results show that the harvester has the potential to scavenge power depending on the proper choice of the tip mass and other parameters. In particular, choosing a tip mass so that the beam is almost buckled gives a relative bandwidth (defined using the half power points) up to twice that of the linear harvester. The maximum power harvested is also significantly greater, once the lower excitation frequencies are accounted for. If the beam is buckled, then the system exhibits the common non-linear system characteristics such as coexisting solution, including chaotic responses. In the buckled configuration, significant power is only harvested if the excitation is sufficient for the system to hop between the potential wells and hence give a large displacement response.

Funding

This study was supported by the Royal Society through International Joint Project No. HP090343. Dr Ali received funding from the Royal Society through a Newton Fellowship. Prof. Adhikari received the support from the Royal Society through a Wolfson Research Merit Award.

References

Ali SF, Adhikari S, Friswell MI, et al. (2011) The analysis of piezomagnetoelastic energy harvesters under broadband random excitations. *Journal of Applied Physics* 109(7): 1–8.

Ali SF and Padhi R (2009) Active vibration suppression of non-linear beams using optimal dynamic inversion. *Proceedings of the Institution of Mechanical Engineers Part I-Journal of Systems and Control Engineering* 223: 657–672.

Anton SR and Sodano HA (2007) A review of power harvesting using piezoelectric materials (2003-2006). *Smart Materials and Structures* 16(3): R1–R21.

Barton DAW, Burrow SG and Clare LR (2010) Energy harvesting from vibrations with a nonlinear oscillator. *Journal of Vibration and Acoustics* 132: 021009, 1–7.

Beeby SP, Tudor MJ and White NM (2006) Energy harvesting vibration sources for microsystems applications. *Measurement Science and Technology* 17(12): R175–R195.

Benjeddou A (2000) Advances in piezoelectric finite element modeling of adaptive structural elements: a survey. *Computers and Structures* 76(4): 347–363.

Bilgen O, Erturk A and Inman DJ (2010) Analytical and experimental characterization of Macro-Fiber Composite actuated thin clamped-free unimorph benders. *Journal of Vibration and Acoustics* 132(5): 051005.

Bilgen O, Wang Y and Inman DJ (2012) Electromechanical comparison of cantilevered beams with multifunctional piezoceramic devices. *Mechanical Systems and Signal Processing* 27: 763–777.

Chee CYK, Tong L and Steven GP (1998) A review on the modeling of piezoelectric sensors and actuators incorporated in intelligent structures. *Journal of Intelligent Material Systems and Structures* 9(1): 3–19.

Chopra I (2002) Review of state of art of smart structures and integrated systems. *AIAA Journal* 40(11): 2145–2187.

Cottone F, Vocca H and Gammaitoni L (2009) Nonlinear energy harvesting. *Physical Review Letters* 102: 080601, 1–4.

Crawley EF (1994) Intelligent structures for aerospace: a technology overview and assessment. *AIAA Journal* 32(8): 1689–1699.

Crawley EF and Anderson EH (1990) Detailed models of piezoceramic actuation of beams. *Journal of Intelligent Material Systems and Structures* 1(1): 4–25.

Crawley EF and De Luis J (1987) Use of piezoelectric actuators as elements of intelligent structures. *AIAA Journal* 25(10): 1373–1385.

Daqaq M (2010) Response of a uni-modal Duffing-type harvesters to random force excitations. *Journal of Sound and Vibration* 329: 3621–3631.

duToit N, Wardle B and Kim S (2005) Design considerations for MEMS-scale piezoelectric mechanical vibration energy harvesters. *Integrated Ferroelectrics* 71: 121–160.

Erturk A, Hoffmann J and Inman DJ (2009) A piezomagnetoelastic structure for broadband vibration energy harvesting. *Applied Physics Letters* 94: 254102, 1–3.

Erturk A and Inman D (2011a) *Piezoelectric Energy Harvesting*. Chichester: John Wiley & Sons Ltd.

Erturk A and Inman DJ (2011b) Broadband piezoelectric power generation on high-energy orbits of the bistable Duffing oscillator with electromechanical coupling. *Journal of Sound and Vibration* 330: 2339–2353.

Erturk A and Inman DJ (2011c) Parameter identification and optimization in piezoelectric energy harvesting: analytical relations, asymptotic analyses, and experimental validations. *Proceedings of the Institution of Mechanical Engineers Part I-Journal of Systems and Control Engineering* 225(I4, SI): 485–496.

Esmailzadeh E and Nakhaie-Jazar G (1998) Periodic behavior of a cantilever beam with end mass subjected to harmonic base excitation. *International Journal of Non-Linear Mechanics* 33(4): 567–577.

Ferrari M, Ferrari V, Guizzetti M, et al. (2008) Piezoelectric multifrequency energy converter for power harvesting in autonomous microsystems. *Sensors and Actuators A: Physical* 142: 329–335.

Ferrari M, Ferrari V, Guizzetti M, et al. (2010) Improved energy harvesting from wideband vibrations by nonlinear piezoelectric converters. *Sensors and Actuators A: Physical* 162: 425–431.

Gammaitoni L, Neri I and Vocca H (2009) Nonlinear oscillators for vibration energy harvesting. *Applied Physics Letters* 94: 164102.

Gammaitoni L, Neri I and Vocca H (2010) The benefits of noise and nonlinearity: extracting energy from random vibrations. *Chemical Physics* 375: 435–438.

High JW and Wilkie WK (2003) *Method of fabricating NASA-standard Macro-Fiber Composite piezoelectric actuators*. Technical Report NASA/TM-2003-212427, ARL-TR-2833. NASA Langley Research Center, Hampton, VA, USA.

Lefeuvre E, Badel A, Benayad A, et al. (2005) A comparison between several approaches of piezoelectric energy harvesting. *Journal de Physique IV* 128: 177–186.

Lefeuvre E, Badel A, Richard C, et al. (2006) A comparison between several vibration-powered piezoelectric generators for standalone systems. *Sensors and Actuators A: Physical* 126(2): 405–416.

Leo DJ (2007) *Engineering Analysis of Smart Material Systems*. John Wiley & Sons, Inc. Hoboken, New Jersey, USA.

Litak G, Friswell MI and Adhikari S (2010) Magnetopiezoelastic energy harvesting driven by random excitations. *Applied Physics Letters* 96(21): 214103.

McInnes C, Gorman D and Cartmell M (2010) Enhanced vibrational energy harvesting using nonlinear stochastic resonance. *Journal of Sound and Vibration* 318(4–5): 655–662.

Mann BP and Owens BA (2010) Investigations of a nonlinear energy harvester with a bistable potential well. *Journal of Sound and Vibration* 329: 1215–1226.

Mann BP and Sims ND (2009) Energy harvesting from the nonlinear oscillations of magnetic levitation. *Journal of Sound and Vibration* 319(1–2): 515–530.

Masana R and Daqaq MF (2011) Relative performance of a vibratory energy harvester in mono- and bi-stable potentials. *Journal of Sound and Vibration* 330: 6036–6052.

Moon FC and Holmes PJ (1979) A magnetoelastic strange attractor. *Journal of Sound and Vibration* 65(2): 275–296.

Nayfeh A and Mook D (1979) *Nonlinear Oscillations*. New York: Wiley-Interscience.

Nayfeh A and Pai P (2004) *Linear and Nonlinear Structural Mechanics*. New Jersey: Wiley Interscience.

Ng T and Liao W (2005) Sensitivity analysis and energy harvesting for a self-powered piezoelectric sensor. *Journal of Intelligent Material Systems and Structures* 16(10): 785–797.

Park C, Walz C and Chopra I (1996) Bending and torsion models of beams with induced-strain actuators. *Smart Materials and Structures* 5: 98–113.

Priya S (2007) Advances in energy harvesting using low profile piezoelectric transducers. *Journal of Electroceramics* 19(1): 165–182.

Quinn DD, Triplett AL, Bergman LA, et al. (2011) Comparing linear and essentially nonlinear vibration-based energy harvesting. *Journal of Vibration and Acoustics* 133: 011001, 1–8.

Ramlan R, Brennan MJ, Mace BR, et al. (2010) Potential benefits of a non-linear stiffness in an energy harvesting device. *Nonlinear Dynamics* 59: 545–558.

Renno JM, Daqaq MF and Inman DJ (2009) On the optimal energy harvesting from a vibration source. *Journal of Sound and Vibration* 320(1–2): 386–405.

Roundy S (2005) On the effectiveness of vibration-based energy harvesting. *Journal of Intelligent Material Systems and Structures* 16(10): 809–823.

Sebald G, Kuwano H, Guyomar D, et al. (2011) Experimental Duffing oscillator for broadband piezoelectric energy harvesting. *Smart Materials and Structures* 20: 102001, 1–10.

Shu YC and Lien IC (2006a) Analysis of power output for piezoelectric energy harvesting systems. *Smart Materials and Structures* 15(6): 1499–1512.

Shu YC and Lien IC (2006b) Efficiency of energy conversion for a piezoelectric power harvesting system. *Journal of Micromechanics and Microengineering* 16(11): 2429–2438.

Shu YC, Lien IC and Wu WJ (2007) An improved analysis of the SSHI interface in piezoelectric energy harvesting. *Smart Materials and Structures* 16(6): 2253–2264.

Sodano H, Inman D and Park G (2004) A review of power harvesting from vibration using piezoelectric materials. *The Shock and Vibration Digest* 36: 197–205.

Stanton SC, McGehee CC and Mann BP (2010) Nonlinear dynamics for broadband energy harvesting: investigation of a bistable piezoelectric inertial generator. *Physica D: Nonlinear Phenomena*, 239(10): 640–653.

Wang L, Kazmierski TJ, Al-Hashimi BM, et al. (2009) An automated design flow for vibration-based energy harvester systems. In: *Design, automation and test in Europe conference and exhibition*, Nice, France, 20–24 April, vols 1–3, pp. 1391–1396. IEEE.

Wilkie WK, Bryant GR, High JW, et al. (2000) Low-cost piezocomposite actuator for structural control applications. In: *SPIE 7th annual international symposium on smart structures and materials*, Newport Beach, CA, 5–9 March, vol. 3991. SPIE.

Zavodney L and Nayfeh A (1989) The nonlinear response of a slender beam carrying a lumped mass to a principal parametric excitation: theory and experiment. *International Journal of Non-Linear Mechanics* 24(2): 105–125.